

pubs.acs.org/JPCL Letter

# A Computational Study of the Electronic Energy and Charge Transfer Rates and Pathways in the Tetraphenyldibenzoperiflanthene/Fullerene Interfacial Dyad

Alexander Schubert, Srijana Bhandari, Eitan Geva,\* and Barry D. Dunietz\*



Cite This: J. Phys. Chem. Lett. 2023, 14, 9569–9583



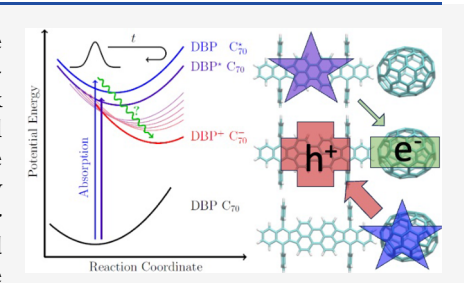
**ACCESS** I

III Metrics & More

Article Recommendations

Supporting Information

**ABSTRACT:** The electronic transition rates and pathways underlying interfacial charge separation in tetraphenyldibenzoperiflanthene:fullerene (DBP: $C_{70}$ ) blends are investigated computationally. The analysis is based on a polarization-consistent framework employing screened range-separated hybrid functional in a polarizable continuum model to parametrize Fermi's golden rule rate theory. The model considers the possible transitions within the 25 lowest excited states of a DBP: $C_{70}$  dyad that are accessible by photoexcitation. The different identified pathways contributing to charge carrier generation include electron and hole transfer and backtransfer, exciton transfer, and internal relaxation steps. The larger density of states of  $C_{70}$  appears to explain the previously observed larger efficiency for charge separation through hole transfer



mechanism. We also analyze the validity of the high-temperature and short-time semiclassical approximations of the FGR theory, where both overestimated and underestimated Marcus theory based constants can be affected.

he performance of organic photovoltaic devices is based on their ability to efficiently generate charge carriers following the absorption of solar radiation. In these systems, charge carrier generation results from a cascade of processes triggered by photoabsorption. For example, solar radiation absorption by the donor material can lead to the creation of donor excitons that migrate to the donor-acceptor interface, where donor-toacceptor electron transfer could take place. This is followed by the transport and collection of the electron and hole to accomplish the conversion of solar energy into electrical energy. Thus, optimizing the interfacial charge transer (CT) step can enhance the overall conversion efficiency.<sup>1,2</sup> As a result, the design of organic photovoltaic (OPV) devices is often based on blending donor and acceptor materials to increase the interfacial cross section for the electron transfer step and reduce the exciton diffusion length.

While donor-based excitons represent one pathway for the generation of free charge carriers, acceptor-based excitons can play a similar role. More specifically, acceptor excitons can migrate to the donor—acceptor interface, where acceptor-to-donor *hole transfer* could occur, which is equivalent to a donor-to-acceptor electron transfer. Indeed, the effectiveness of the pathway that starts with acceptor-based excitons is consistent with the experimental observation, made in several blended heterogeneous junctions (BHJs), that the efficiency can also be *increased* by *reducing* the donor content.<sup>3–7</sup> In particular tetraphenyldibenzoperiflanthene:fullerene (DBP:C<sub>70</sub>, Figure 1 top left panel) blends have been shown to give rise to peak OPV performance at 1:8 donor/acceptor dilution ratio.<sup>4</sup> Another recent study that combined two-dimensional electronic spec-

troscopy (2DES) with electronic structure calculations provided further evidence for the effectiveness of the donor exciton and hole transfer pathway as an effective mechanism for the formation of free charge carriers in this system.<sup>7</sup>

A schematic view of the various electronic energy and charge transfer processes that can occur in DBP: $C_{70}$  is provided in Figure 1. Interfacial CT can follow either electron or hole transfer pathways that may be preceded by Förster resonant energy transfer, intramolecular electronic relaxation, or transient charge recombination (backtransfer).

More specifically, given a donor or an acceptor exciton at the donor–acceptor interface, multiple pathways can lead to the final CT states, denoted CT1 and CT2. These pathways can be qualitatively described in terms of transitions between localized molecular orbitals (MOs) comprising the highest occupied MOs (H) and lowest unoccupied MOs (L) of the donor and acceptor molecules as well as some MOs below H and above L. The main steps underlying these pathways are described in more detail below.

Electron transfer occurs after donor excitation and corresponds to electron transfer from L of the donor molecule (DBP) to L of the acceptor molecule ( $C_{70}$ ) (see panel a in Figure 1). Alternatively, hole transfer occurs after acceptor excitation and

Received: July 13, 2023 Accepted: October 2, 2023 Published: October 20, 2023





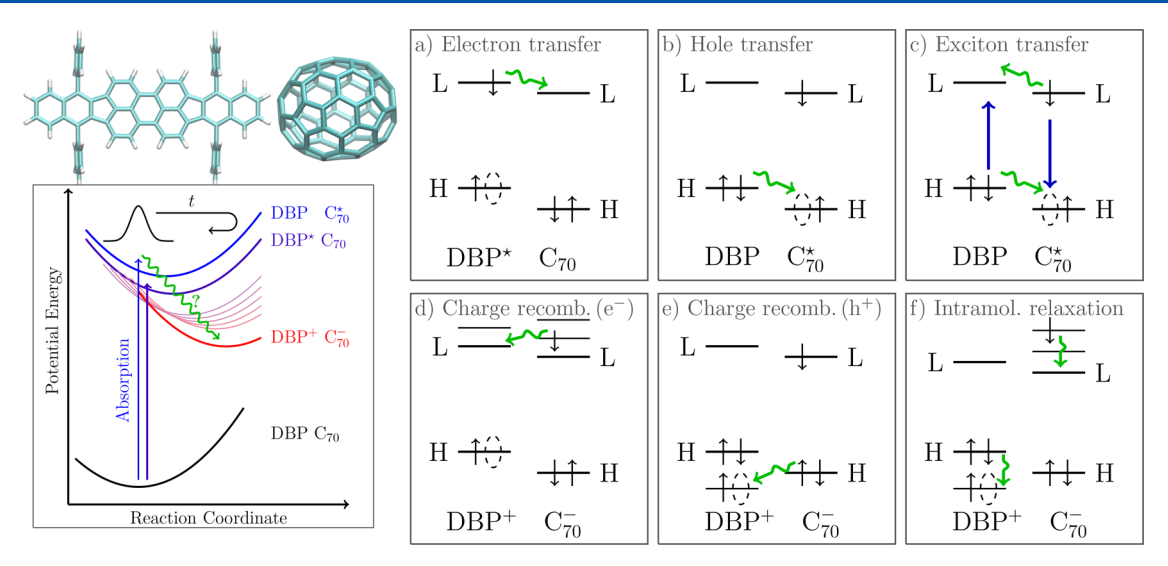


Figure 1. Upper left: The molecular structures of DBP and  $C_{70}$ . Lower left: Upon absorption (blue arrows) *bright* states are excited either localized on DBP or  $C_{70}$ , followed by nonradiative electronic transitions (green arrows) toward the formation of long-lived charge transfer (CT) states. Right panels (a–f): Individual types of nonradiative electronic transitions can be identified as (a) electron transfer, (b) hole transfer, (c) exciton transfer, (d) electron backtransfer, (e) hole backtransfer, and (f) intramolecular relaxation (see main text for a more detailed discussion).

corresponds to electron transfer from H of the donor molecule (DBP) to H of the acceptor molecule ( $C_{70}$ ) (see panel b in Figure 1).

Another type of state involved in the cascade of events following photoexcitation is excited CT states, which correspond to the excess electron occupying a higher than L MO of the acceptor  $C_{70}$  (see panel d in Figure 1) or the hole occupying a lower than H MO of the donor DBP (see panel e in Figure 1). Those states can relax via a CT recombination process to form a neutral dyad with either an excited donor or acceptor (see panels d and e in Figure 1, respectively). It should be noted that excited CT states where the excess electron occupies a higher than L MO of the donor or the hole occupies a lower than H MO of the acceptor are much higher in energy and therefore are assumed to be inaccessible.

Another possible process corresponds to exciton transfer (see panel c in Figure 1). This can happen via two distinctly different mechanisms. The so-called Dexter-type exciton transfer <sup>9,10</sup> corresponds to simultaneous transfer of an electron and a hole from acceptor to donor (see green arrows in panel c of Figure 1). Alternatively, the so-called Förster resonant exciton transfer (FRET)<sup>11</sup> type exciton transfer corresponds to the simultaneous de-excitation of the acceptor and excitation of the donor (see blue arrows in panel c of Figure 1).

Yet another type of process corresponds to intramolecular electronic energy relaxation, whereby an electron occupying a higher than L acceptor MO relaxes to the acceptor's L MO or a hole occupying a lower than H donor MO is filled by electron transfer from the donor's L MO (see blue arrows in panel f in Figure 1)

Our computational approach to modeling the kinetics underlying interfacial CT in DBP: $C_{70}$  combines electronic structure calculations with a fully quantum-mechanical rate theory based on equilibrium Fermi's golden rule (FGR). This approach makes it possible to identify the different pathways leading to charge separation and the interplay between them. In addition, we also compare FGR rate constants to a hierarchy of more approximate semiclassical variations, which leads to Marcus theory as the most approximate semiclassical variant. As we show below, while Marcus theory is often reliable,

Marcus rate constants for some of the transitions in this system can deviate from the FGR-based rate constants by several orders of magnitude.

The electronic structure protocol we use is based on DFT with a screened range separated hybrid (SRSH) functional that addresses dielectric screening by the solid state environment in a polarization-consistent manner. <sup>15,16</sup> Combining SRSH with the polarizable continuum model (PCM) is important for obtaining the correct order of the energy levels that correspond to the neutral and CT excited electronic states. SRSH-PCM was previously used successfully to analyze spectral trends in organic systems <sup>7,17–19</sup> including fullerenes. <sup>19</sup> We also point out the high density of states in fullerene due to its high symmetry, which calls for an electronic structure level of theory that can capture the correct order of energy levels in such a case.

### **■ THEORY AND METHODS**

Electronic Structure Calculations. Within our model, interfacial CT can occur via multiple pathways that consist of multiple transitions between electronic states of different electronic character. The state-to-state rate constants underlying those pathways strongly depend on the relative energies of the states and therefore require an accurate method for calculating the energies of excited electronic states, including excited CT states. Traditional DFT including that based on hybrid functionals with a constant weight of the exact Fock exchange contribution is affected by the fundamental-gap caveat.<sup>20-26</sup> Recently developed range-separated hybrid (RSH) functionals based on a generalized Kohn-Sham formulation 25,27-33 give rise to gas phase frontier orbital energies that agree with the ionization potential (IP) and electron affinity (EA), 34-37 which is necessary for obtaining accurate excited CT states' energies via time-dependent DFT (TDDFT) calculations.

RSH functionals partition the exchange energy contribution into a short-range (SR) term, and a long-range (LR) term:

$$\frac{1}{r} = \frac{\alpha + \beta \operatorname{erf}(\omega r)}{r} + \frac{1 - [\alpha + \beta \operatorname{erf}(\omega r)]}{r} \tag{1}$$

where erf denotes the error function, r is the interelectronic distance, and  $\omega$  is a range-separation parameter. The coefficients  $\alpha$  and  $\beta$  determine the fraction of semilocal exchange and Fock exchange in the respective domains. More specifically, the amount of Fock exchange scales with  $\alpha$  in the SR and with  $(\alpha+\beta)$  in the LR, and, therefore, the corresponding semilocal density functional SR and LR contributions are given by  $(1-\alpha)$  and  $(1-\alpha-\beta)$ , respectively. The RSH exchange-correlation (XC) energy is therefore given by

$$E_{\text{XC}}^{\text{RSH}}(\omega) = E_{\text{C,DF}} + \alpha E_{\text{X,F}}^{\text{SR}}(\omega) + (1 - \alpha) E_{\text{X,DF}}^{\text{SR}}(\omega)$$
$$+ (\alpha + \beta) E_{\text{X,F}}^{\text{LR}}(\omega) + (1 - \alpha - \beta) E_{\text{X,DF}}^{\text{LR}}(\omega)$$
(2)

where X and C denote exchange and correlation and F and DF indicate Fock exchange and the semilocal density functional, respectively.

Importantly, the energies of excited CT electronic states can be strongly affected by the presence of a polarizable condensed phase environment. In our approach, PCM is invoked to capture such condensed phase effects. However, while RSH functionals have been shown to achieve high accuracy in predicting ionization energies and electron affinities in the gas phase, the orbital gap in RSH-PCM tends to remain close to the gas phase gap and would therefore be overestimated in the condensed phase. To address this caveat, we employ a screened RSH (SRSH) framework to achieve a polarization-consistent framework. 15,16,44,45

To account for the appropriate polarization effects of the environment, Refaely-Abramson et al. introduced a screening of the asymptotic potential through the dielectric constant  $\epsilon_0$ , such that the interelectronic potential,  $r^{-1}$ , takes the form  $(\epsilon_0 r)^{-1}$ . This is achieved by setting  $\alpha + \beta = \epsilon_0^{-1}$  [see eq 1]. In addition to the dielectric screening of LR exchange contributions, environmental polarizing effects are accounted for via PCM. Thus, dielectric screening is addressed consistently by the selfconsistent reaction field responding to the dielectric constant,  $\epsilon_0$ , within the PCM and by damping the LR exchange in the SRSH functional. The combined SRSH-PCM approach has been shown in previous work to significantly improve RSH-PCM calculations of fundamental gaps<sup>15</sup> and of excited states<sup>7,17–19,45–49</sup> including CT states in organic semiconductors. 16 SRSH-PCM was also recently successfully applied to interpret the spectral signature of interfacial CT in DBP:C70 blends.7

In this work, we employ the SRSH-PCM framework to obtain electronically excited donor—acceptor interfacial states. To this end, DFT and TDDFT calculations were performed on single DBP and  $C_{70}$  molecules, as well as on the DBP: $C_{70}$  dyad. As the primary focus of this work is on the processes occurring in the DBP: $C_{70}$  1:8 blend, in all calculations PCM is employed with the dielectric constant of the  $C_{70}$  thin film ( $\epsilon_0$  = 3.75) and an optical dielectric constant of  $\epsilon_{\infty}$  = 1.67 affecting the TDDFT linear response equations.

The SRSH-PCM framework is based on the  $\omega$ PBE-h functional. The range-separation parameter  $\omega$  was obtained through optimal tuning according to the  $J^2$  scheme. Accordingly  $\omega$  has been set to 0.18 bohr<sup>-1</sup> for the C<sub>70</sub> single molecule and 0.11 bohr<sup>-1</sup> for the DBP single molecule. The latter value was also found to yield very low  $J^2$  values for the DBP:C<sub>70</sub> dyad and is used in all dyad state calculations. The functional parameter  $\alpha$  has been kept at the widely used value of 0.2.

All equilibrium geometries were obtained using the dispersion-corrected RSH functional  $\omega$ B97X-D with the 6-31G\* basis set. 51,52 Normal mode frequencies and eigenvectors were calculated at the same level of theory for the electronic groundstate at its equilibrium geometry. Orbitals and excited state properties—i.e. excitation energies  $\{E_n^x\}$ , oscillator strengths  $\{\Omega_n\}$ , and attachment and detachment densities—were calculated via the SRSH-PCM framework. Charge differences  $\{dQ_n\}$ between the DBP and the  $C_{70}$  molecule in the dyad system were calculated based on Mulliken charges. Atomic Mulliken charges were used to parametrize the calculation of the electronic coupling elements  $\{V_{mn}\}$  between excited dyad states m and n. To this end, a multistate generalization of the fragment-charge difference method was used,<sup>53</sup> abbreviated below as msFCD.<sup>5</sup> This method does not require an arbitrary selection of diabatic states and instead generates charge-transfer and locally excited state subspaces based on the eigenvalues of the charge difference matrix. All electronic structure calculations were performed using the Q-Chem software package. St

Coupling elements were assumed to be constant within the Condon approximation and are determined at the dyad's optimized ground state geometry, assuming that the normal modes are the same in the ground and excited states. It should be noted that non-Condon effects, for example in the form of the linear Herzberg-Teller coupling, can have a significant effect on electronic transition rates. <sup>56,57</sup> We also note that non-Condon effects can be accounted for within a Fermi's Golden Rule framework. 58,59 However, for the system under consideration in this paper, accounting for non-Condon effects would require performing geometry optimizations for the 25 diabatic excited states under consideration, which would be computationally demanding as well as challenging due to the prevalence of curve crossings. Similarly, even though accounting for Duschinski rotations,60 within the FGR framework is possible in principle, \$6,61 it would also dramatically increase the computational cost. Thus, given the complexity of the system and the consistency of our calculations with experimentally available data, we believe that starting out with the Condon approximation and neglecting Duschinski rotations are reasonable choices, at least until new experimental data emerge for this system that would justify incorporating such effects into the model.

**Rate Theory.** Fermi's Golden Rule. The high symmetry of the  $C_{70}$  molecule leads to a high number of excited states within the optical excitation range. Although many of these states are dark and therefore cannot be reached via photoexcitation, they can be occupied transiently via radiationless transitions en route to the final target CT states. As a result, the rates of populating and depopulating those intermediate states have a significant effect on the overall efficiency of the charge separation process (see below).

Overall, we found that there were 25 excited electronic states within the experimental optical range (Table 1). The dynamics of the populations of those 25 states is assumed to be described by the following master equation:

$$\frac{\mathrm{d}p_n(t)}{\mathrm{d}t} = \sum_{m \neq n} \left[ k_{nm} p_m(t) - k_{mn} p_n(t) \right] \tag{3}$$

where  $p_n(t)$  is the time-dependent population of the *n*th electronic excited state and  $k_{mn}$  is the rate constant for a transition from state *n* to state *m*.

Table 1. Lowest 25 Dyad Excited States and Their Properties: Excitation Energy  $(E_n^x)$ , Oscillator Strength  $(\Omega_n)$ , and Mulliken Charge Difference between DBP and  $C_{70}$   $(dQ_n)^a$ 

	_				
n	$E_n^{\rm x}/{\rm eV}$	$\Omega_n$	$dQ_n/e$	b/d	$\chi_n$
1	1.473	0.000	2.0	dark	CT
2	1.496	0.000	2.0	dark	CT
3	1.675	0.001	2.0	dark	CT
4	2.051	0.009	2.0	dark	CT
5	2.105	0.850	0.2	bright	DBP*
6	2.135	0.002	0.1	dark	C70*
7	2.153	0.004	0.1	dark	C70*
8	2.209	0.001	0.1	dark	C70*
9	2.216	0.001	0.1	dark	C70*
10	2.272	0.002	0.1	dark	C70*
11	2.298	0.006	0.1	dark	C70*
12	2.311	0.020	1.8	bright	CT
13	2.320	0.004	1.9	dark	CT
14	2.378	0.019	0.2	bright	C70*
15	2.384	0.001	1.8	dark	CT
16	2.404	0.001	1.9	dark	CT
17	2.408	0.015	0.6	bright	C70*
18	2.415	0.003	0.6	dark	C70*
19	2.443	0.023	0.2	bright	C70*
20	2.451	0.001	1.4	dark	CT
21	2.454	0.022	1.5	bright	CT
22	2.481	0.059	0.1	bright	C70*
23	2.536	0.002	1.4	dark	CT
24	2.587	0.002	1.4	dark	CT
25	2.592	0.002	1.2	dark	CT
a					

"The states' predominant characters  $\chi_n$  are assigned by attachment/ detachment density analysis (see Figure 4) and by their oscillator strengths as bright  $(\Omega_n > 0.01)$  or dark  $(\Omega_n < 0.01)$ .

It should be noted that the validity of the populations-only Markovian master equation with rate constants based on equilibrium FGR used in this work relies on several assumptions. More specifically, nonequilibrium, non-Markovian, and coherent effects are assumed to be negligible. Given the complexity of the system and the consistency of our calculations with experimentally available data, we believe that the level of theory as implemented is justified, at least until new experimental data emerge for this system that would call for extensions of the type alluded to above (e.g., see refs 62-66).

The  $25 \times (25-1) = 600$  transition rate constants between the aforementioned 25 excited electronic states were calculated based on equilibrium FGR rate theory, as well as a hierarchy of semiclassical approximations that can be derived from it, which leads to the Marcus theory rate constant as the most approximate semiclassical variant. It should be noted that the equilibrium FGR rate theory used here is based on treating the electronic coupling as a small perturbation within the framework of second-order perturbation theory and assuming that the nuclear degrees of freedom (DOFs) are harmonic and start out at thermal equilibrium on the initial electronic state's potential energy surface. 12-14 A similar approach has been benchmarked and employed by us to model the correlation between interfacial structure and CT rate in the DBP: $C_{70}$  system, 7,13,67 as well as other closely related systems.  $C_{70}$ 

Within the equilibrium FGR rate theory, the  $m \leftarrow n$  transition rate constant is given by

$$k_{mn}^{\xi} = \frac{|V_{mn}|^2}{\hbar^2} \int_{-\infty}^{\infty} dt \ F(t) e^{i\Delta E_{mn}t/\hbar} \kappa_{mn}^{\xi}(t)$$
(4)

where  $\xi$  indicates the level of theory within the aforementioned hierarchy of semiclassical approximations, and F(t) is a Gaussian time-window,  $F(t) = \exp(-t^2/\tau^2)$ , ensuring numerical convergence. Here F(t) is set with a time constant of  $\tau = 100$  fs. This time-window function can be thought of as accounting for the effect of the reorganization in the dyad's environment. The time window employed in this work corresponds to a rather small outersphere reorganization energy of  $E_r^{ex} = \hbar^2/(k_BT \tau^2) = 1.7$  meV, which is consistent with the fact that the solid state environment in a thin film is rather rigid.

For the fully quantum-mechanical FGR treatment ( $\xi$  = FGR),  $\kappa_{mn}^{\xi}(t) \rightarrow \kappa_{mn}^{\rm FGR}(t)$  is given by  $^{12-14}$ 

$$\kappa_{mn}^{\text{FGR}}(t) = \exp\left\{\sum_{\alpha} -S_{\alpha,mn}(2n_{\alpha} + 1) + S_{\alpha,mn}[(n_{\alpha} + 1)e^{-i\omega_{\alpha}t} + n_{\alpha}e^{i\omega_{\alpha}t}]\right\}.$$
(5)

Equation 5 relies on the assumption that the nuclear DOFs are harmonic and that the harmonic potential energy surfaces that correspond to different electronic states are given in terms of the same set of normal mode coordinates and are identical except for a shift in equilibrium energy and geometry. The summation in eq 5 is over the normal modes, the frequencies of which are given by  $\{\omega_{\alpha}\}$ .  $\{n_{\alpha}=(\exp\{\hbar\ \omega_{\alpha}/k_{\rm B}T\}-1)^{-1}\}$  in eq 5 are the normal modes' thermal occupancies at temperature T (assumed to be room temperature, with  $k_{\rm B}$  the Boltzmann constant).  $V_{mn}$  in eq 4 is the electronic states.  $\Delta E_{mn}$  in eq 4 is the energy difference between the equilibrium energies of the initial and final states (which is also equal to the *negative* of the reaction energy or driving force):

$$\Delta E_{mn} = E_n^{\text{eq}} - E_m^{\text{eq}} \tag{6}$$

The corresponding difference in equilibrium geometries is given by the displacement vectors:

$$\mathbf{D}_{mn} = \mathbf{R}_n - \mathbf{R}_m \tag{7}$$

Projecting the displacement vectors onto the normal mode eigenvectors gives rise to the Huang-Rhys factors (HRFs), which are defined by (see eq 5)

$$S_{\alpha,mn} = \frac{\omega_{\alpha}}{2\hbar} (\mathbf{e}_{\alpha} \cdot \mathbf{D}_{mn})^2 \tag{8}$$

where  $\mathbf{e}_{\alpha}$  is the normalized displacement of the equilibrium geometry along the  $\alpha$ -th normal mode's relative to the groundstate equilibrium geometry  $\mathbf{R}_0$ . Finally, we note that the reorganization energy for the  $m \leftarrow n$  transition is given by

$$E_{mn}^{r} = \sum_{\alpha} \hbar \omega_{\alpha} S_{\alpha,mn} \tag{9}$$

The size of the reorganization energy relative to the absolute value of the reaction energy determines whether a transition rate constant falls into the normal region ( $E^{\rm r}_{mn} \geq |\Delta E_{mn}|$ ) or the inverted region ( $E^{\rm r}_{mn} < |\Delta E_{mn}|$ ). Total affected reorganization energy corresponds to both internal and outersphere contributions:  $E^{\rm r}_{mn} + E^{\rm ex}_{\rm r}$ .

Limit Cases and Semiclassical Approximation. Starting with the quantum-mechanically exact equilibrium FGR expression in eqs 4 and 5, a hierarchy of semiclassical

approximations can be derived, with the most approximate variant corresponding to Marcus theory. The first approximation corresponds to the high-temperature/low-frequency limit, i.e.  $k_{\rm B}T\gg\hbar\omega_{\alpha}$  of  $\kappa_{mn}^{\rm FGR}(t)$ . In this limit,  $n_{\alpha}\approx k_{\rm B}T/\hbar\omega_{\alpha}$ . Substituting this result in eq 5, we obtain the following high-temperature limit approximation (labeled  $\xi={\rm hT1}$ ):

$$\kappa_{mn}^{\text{hT1}}(t) = \exp\left\{\sum_{\alpha} -S_{\alpha,mn} \left(\frac{2k_{\text{B}}T}{\hbar\omega_{\alpha}} + 1\right) + S_{\alpha,mn} \left[\left(\frac{k_{\text{B}}T}{\hbar\omega_{\alpha}} + 1\right) e^{-i\omega_{\alpha}t} + \frac{k_{\text{B}}T}{\hbar\omega_{\alpha}} e^{i\omega_{\alpha}t}\right]\right\}.$$
(10)

Noting that the high-temperature approximation also implies that  $k_{\rm B}T/\hbar\omega_{\alpha}\gg 1$ ,  $\kappa_{mn}^{\rm hT1}(t)$  can be further simplified into the following alternative version of the high temperature limit: (labeled  $\xi={\rm hT2}$ ):

$$\kappa_{mn}^{\rm hT2}(t) = \exp\left\{\sum_{\alpha} S_{\alpha,mn} \left[ \frac{2k_{\rm B}T}{\hbar\omega_{\alpha}} (\cos(\omega_{\alpha}t) - 1) - i \right] \right\}$$

$$\sin \omega_{\alpha}t$$
(11)

Another interesting limit is the short-time limit, which corresponds to the assumption that the correlation function  $\kappa_{mn}^{\rm FGR}(t)$  in eq 5 is short-lived. In this case, a Taylor expansion of  ${\rm e}^{\pm i\,\omega_a t}$  in eq 5 to second order in  $\omega_a t$  leads to the following short-time limit (labeled  $\xi={\rm st}$ ):

$$\kappa_{mn}^{\text{st}}(t) = \exp\left\{\sum_{\alpha} S_{\alpha,mn} \left[ -i\omega_{\alpha}t - \frac{1}{2}(1 + 2n_{\alpha})\omega_{\alpha}^{2}t^{2} \right] \right\}$$
(12)

Since  $\kappa_{mn}^{\rm st}(t)$  is a Gaussian function of time, in this case, the time integral in eq. 4 can be obtained in closed form:

$$k_{mn}^{\text{st}} = \frac{|V_{mn}|^2}{\hbar^2} \sqrt{\frac{\pi}{A_{mn}}} \exp\left\{-\frac{(\Delta E_{mn} - E_{mn}^{\text{r}})^2}{4\hbar^2 A_{mn}}\right\}$$
(13)

with  $A_{mn} = \frac{1}{2} \sum_{\alpha} (2n_{\alpha} + 1) S_{\alpha,mn} \omega_{\alpha}^2$  and  $E_{mn}^{\rm r}$  as defined in eq 9. Combining the short-time approximation with the hT2 approximation implies that  $A_{mn} \approx k_{\rm B} T E_{mn}^{\rm r} / \hbar^2$ , and reduces eq 13 into the well-known Marcus theory rate constant  $(\xi = {\rm M})$ :

$$k_{mn}^{M} = \frac{|V_{mn}|^2}{\hbar} \sqrt{\frac{\pi}{k_{\rm B} T E_{mn}^{\rm r}}} \exp\left\{-\frac{(\Delta E_{mn} - E_{mn}^{\rm r})^2}{4k_{\rm B} T E_{mn}^{\rm r}}\right\}$$
(14)

We also note that the activation energy for the  $m \leftarrow n$  transition is given by

$$E_{mn}^{A} = \frac{(\Delta E_{mn} - E_{mn}^{r})^{2}}{4E_{mn}^{r}} \tag{15}$$

Our choice to include a comparison to the hT and st approximations was motivated by the fact that they are the approximations underlying Marcus theory. It should be noted that other approximations exist that would also be worthwhile to consider for the system under consideration. Of particular interest are the stationary phase approximations. That were reported to be more accurate than the st and hT approximations.

Numerical Simulation. In practice, it was not feasible to calculate equilibrium FGR rate constants based on eq 4 and its

approximate versions in eqs 10–14 for all 600 electronic transitions. Instead, those rate constants were calculated based on single molecule properties following the protocol described below.

We start out by noting that the rate constants  $\{k_{mn}^{\xi}\}$  depend on the equilibrium energies of the initial and final states,  $E_n^{eq}$  and  $E_m^{eq}$ , respectively [through  $\Delta E_{mn}$ , eq 6], and the corresponding equilibrium geometries,  $\mathbf{R}_n$  and  $\mathbf{R}_m$  (through the HRFs, eqs 7 and 8). In practice, geometry optimization of all relevant electronically excited states was not feasible due to the high density of states and multiple curve crossings. Instead, reaction energies,  $\{\Delta E_{mn}\}$ , and HRFs,  $\{S_{\alpha,mn}\}$ , were evaluated based on calculations performed on a single DBP or C<sub>70</sub> molecules. This amounts to neglecting contributions of intermolecular modes to the HRFs, which is a reasonable approximation since the majority of modes are intramolecular and intermolecular interactions are significantly weaker. We point out that the reliability of mapping structural displacements to combinations of monomer contributions was confirmed for cases where dyad geometries can be readily identified. More specifically, both the lowest absorbing dyad state, which is localized on the donor, and the lowest dyad excited state, which is a dark CT state, were found to give rise to reorganization energies that are reproduced well by corresponding monomer energies.

Mapping the interfacial states to combination of single-molecule states is based on attachment/detachment densities calculated at the ground-state geometries,  $\mathbf{R}_0$ . Here, the detachment density corresponds to the depletion in the groundstate electron density due to excitation into state n, and the attachment density corresponds to the enhancement of the groundstate electron density due to excitation into state n. A comparison to single-molecule MOs allows one to assign each dyad state n a predominant character  $\chi_n$  of either a localized DBP excitation (DBP\*), a localized  $\mathbf{C}_{70}$  excitation (C70\*), or a forward charge transfer state (CT), where a DBP MO is depopulated and a  $\mathbf{C}_{70}$  MO is populated (see Table 1). It should be noted that backward CT states from  $\mathbf{C}_{70}$  to DBP are outside the accessible energy range.

For the purpose of mapping the reorganization energy, we performed geometry optimizations on the single molecules of DBP and  $C_{70}$  in their electronic groundstate ( $\mathbf{R}_{0}^{\mathrm{DBP}}$  and  $\mathbf{R}_{0}^{\mathrm{C70}}$ , respectively), their first excited state ( $\mathbf{R}_{1}^{\mathrm{DBP}}$  and  $\mathbf{R}_{1}^{\mathrm{C70}}$ , respectively), and the DBP cationic and  $C_{70}$  anionic states ( $\mathbf{R}_{+}^{\mathrm{DBP}}$  and  $\mathbf{R}_{-}^{\mathrm{C70}}$ , respectively). Each dyad state bears a character,  $\chi_{n} \in \{\mathrm{DBP}^{*}, \mathrm{C70}^{*}, \mathrm{and} \, \mathrm{CT}\}$  with displacement vectors  $\mathbf{D}^{\chi_{n}}$  that are calculated with respect to the groundstate geometries:

$$\mathbf{D}^{\mathrm{DBP}^*} = \mathbf{R}_{\mathrm{l}}^{\mathrm{DBP}} - \mathbf{R}_{\mathrm{0}}^{\mathrm{DBP}} \tag{16}$$

$$\mathbf{D}^{\text{C70*}} = \mathbf{R}_{1}^{\text{C70}} - \mathbf{R}_{0}^{\text{C70}} \tag{17}$$

$$\mathbf{D}^{\text{CT}} = (\mathbf{R}_{+}^{\text{DBP}} - \mathbf{R}_{0}^{\text{DBP}}) + (\mathbf{R}_{-}^{\text{C70}} - \mathbf{R}_{0}^{\text{C70}})$$
 (18)

HRFs,  $\{S_{\alpha}^{\chi_n}\}$ , are obtained via projection onto the set of normal modes  $\{\omega_{\alpha}\}$  of the two single molecules:

$$S_{\alpha}^{\chi_{n}} = \frac{\omega_{\alpha}}{2\hbar} (\mathbf{e}_{\alpha} \cdot \mathbf{D}^{\chi_{n}})^{2} \tag{19}$$

so that for each state the reorganization energy is approximated through its character  $\chi_n$ :

$$E_n^{\rm r} \approx E_{\chi_n}^{\rm r} = \sum_{\alpha} \hbar \omega_{\alpha} S_{\alpha}^{\chi_n} \tag{20}$$

Thus, the reorganization energy of state n,  $E_n^r$  is determined by the character of state  $\chi_n$ ,  $E_{\chi_n^r}$ .

The energetic minimum  $E_n^{\text{eq}}$  of a dyad state n with character  $\chi_n$  is then approximated by its excitation energy at the groundstate geometry  $E_n^{\text{x}}$  and its associated reorganization energy  $E_n^{\text{r}}$  as illustrated in Figure 2a:

$$E_n^{\text{eq}} = E_n^{\text{x}} - E_n^{\text{r}} \tag{21}$$

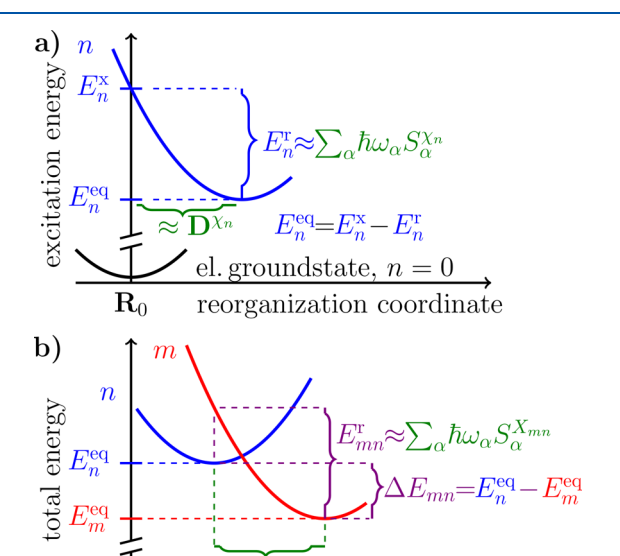


Figure 2. A schematic view of the approximations underlying the calculation of the energy difference,  $\Delta E_{mnn}$  and the displacement,  $\mathbf{D}_{mnn}$  (violet color). The excitation energies  $E^{\mathbf{x}}_{n/m}$  (blue/red) are determined from dyad state calculations, whereas displacements,  $\mathbf{D}^{\chi_n}$  and  $\mathbf{D}^{\chi_{mnn}}$ , normal modes,  $\omega_a$ , and thus HRFs,  $\mathbf{S}^{\chi_n}_\alpha$  and  $\mathbf{S}^{\chi_{mnn}}_\alpha$ , are taken from single molecule calculations (green) with the different types introduced in the main text.

transition coordinate

 $\mathbf{D}_{mn} \approx \mathbf{D}^{X_{mn}}$ 

Thus, the energy difference,  $\Delta E_{mn}$ , eq 6, is obtained from dyad excitation energies and the associated single molecule normal modes and displacements as shown in Figure 2b. In practice, only rate constants  $k_{mn}^{\xi}$  for positive energy differences (downhill processes), i.e.,  $\Delta E_{mn} \geq 0$ , are calculated based on eq 4. Transition rates in the opposite direction are calculated by invoking a detailed balance:

$$k_{nm}^{\xi} = k_{mn}^{\xi} e^{-\Delta E_{mn}/k_{\rm B}T} \tag{22}$$

Importantly, the HRFs for transitions between excited states,  $m \leftrightarrow n$ ,  $\{S_{\alpha,mn}\}$ , are based on the pair of state characters  $(\chi_m, \chi_n)$ . Accordingly, process types  $X_{mn} \in \{A,B,C,D,E,F,G\}$  are identified as illustrated in Figure 3. For these seven process types,  $\{X_{mn}\}$ , displacement vectors  $\mathbf{D}^{X_{mn}}$  are approximated by combining single molecule displacements as follows

$$\mathbf{D}^{\mathbf{A}} = \mathbf{D}^{\mathbf{DBP}^*} + \mathbf{D}^{\mathbf{C70}^*} \tag{23}$$

$$\mathbf{D}^{\mathrm{B}} = \mathbf{D}^{\mathrm{DBP} + *} + \mathbf{D}^{\mathrm{C70}}$$
 (24)

$$\mathbf{D}^{\mathrm{C}} = \mathbf{D}^{\mathrm{DBP}+} + \mathbf{D}^{\mathrm{C70-*}} \tag{25}$$

$$\mathbf{D}^{\mathrm{D}} = \mathbf{D}^{\mathrm{F}} = \mathbf{D}^{\mathrm{C70**}} \tag{26}$$

$$\mathbf{p}^{\mathrm{E}} = \mathbf{p}^{\mathrm{DBP}^{**}} \tag{27}$$

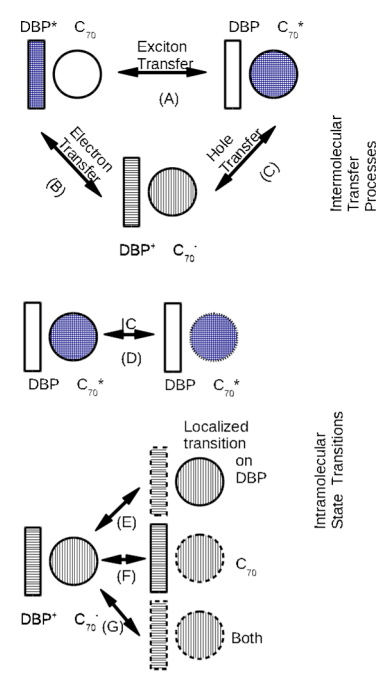


**Figure 3.** Different transition types,  $X_{mn} \in \{A,B,C,D,E,F,G\}$ , in the DBP: $C_{70}$  dyad (see the text for a detailed discussion).

$$\mathbf{p}^{\mathrm{G}} = \mathbf{p}^{\mathrm{DBP}^{**}} + \mathbf{p}^{\mathrm{C70}^{**}} \tag{28}$$

The different HRF distributions are plotted in the Supporting Information, Section S2.

The CT processes B and C relate the charged molecules  $(R_{\scriptscriptstyle +}^{DBP}/R_{\scriptscriptstyle -}^{C70})$  to the excited state geometries  $(R_1^{DBP}/R_1^{C70})$  and therefore require displacements of the single molecules with respect to ground state and excited state geometries:

$$\mathbf{D}^{\mathrm{DBP+}} = \mathbf{R}_{+}^{\mathrm{DBP}} - \mathbf{R}_{0}^{\mathrm{DBP}} \tag{29}$$

$$\mathbf{D}^{\text{C70-}} = \mathbf{R}_{-}^{\text{C70}} - \mathbf{R}_{0}^{\text{C70}} \tag{30}$$

$$\mathbf{D}^{\mathrm{DBP}+*} = \mathbf{R}_{+}^{\mathrm{DBP}} - \mathbf{R}_{\mathrm{I}}^{\mathrm{DBP}} \tag{31}$$

$$\mathbf{D}^{\text{C70-*}} = \mathbf{R}_{-}^{\text{C70}} - \mathbf{R}_{1}^{\text{C70}} \tag{32}$$

In considering higher excited states than the lowest on either molecule, we address also contributions due to intramolecular internal conversion within the manifold of excited states relating higher excited state geometries ( $\mathbf{R}_{1}^{\mathrm{DBP}}/\mathbf{R}_{2}^{\mathrm{C70}}$ ) to the lowest excited state geometries ( $\mathbf{R}_{1}^{\mathrm{DBP}}/\mathbf{R}_{1}^{\mathrm{C70}}$ ):

$$\mathbf{D}^{\text{C70**}} = \mathbf{R}_2^{\text{C70}} - \mathbf{R}_1^{\text{C70}} \tag{33}$$

$$\mathbf{D}^{\mathrm{DBP}^{**}} = \mathbf{R}_{2}^{\mathrm{DBP}} - \mathbf{R}_{1}^{\mathrm{DBP}} \tag{34}$$

Here,  $\mathbf{R}_2^{\mathrm{DBP/C70}}$  indicates the optimized geometry of the second excited state of the DBP and  $C_{70}$  molecule, respectively. Since the reorganization of processes D and F follows in both cases predominantly a depopulation of the  $C_{70}$  L + 1 and population of the L orbital, their displacement is assumed to be the same.

With the molecule displacements  $\mathbf{D}^{X_{mn}}$  specified for each transition type  $X_{mn}$ , reorganization energies can be calculated for the various processes. Among the seven transition types under consideration, we distinguish between (i) intermolecular transfer processes

- (A) exciton transfer
- (B) electron transfer

- (C) hole transfer
- and (ii) intramolecular transition processes
  - (D) internal conversion between C<sub>70</sub>-localized excited states and
- (E-G) between different CT states. The transitions between CT states are further subdivided into three categories, depending on whether
  - (E) only the detachment density differs between the two states, i.e. the electronic transition is localized on the DBP cation
  - (F) only the attachment density differs between the two states, i.e. the electronic transition is localized on the C<sub>70</sub> anion or
  - (G) both detachement and attachment densities undergo significant changes, i.e., the transition is delocalized across the dyad.

We also note that for the CT  $\leftarrow$  CT transitions, i.e.,  $X_{mn} \in \{E, F, G\}$ , displacements were approximated by geometries based on higher excited states of the neutral molecule.

### RESULTS AND DISCUSSION

**Electronic Excited States.** The properties of the 25 excited states of the dyad that fall within the experimentally relevant spectral range are listed in Table 1. The state character,  $\chi_n$ , is assigned to the corresponding attachment and detachment densities in the context of the MOs of the single molecules. The densities are shown for five of those states in Figure 4, and

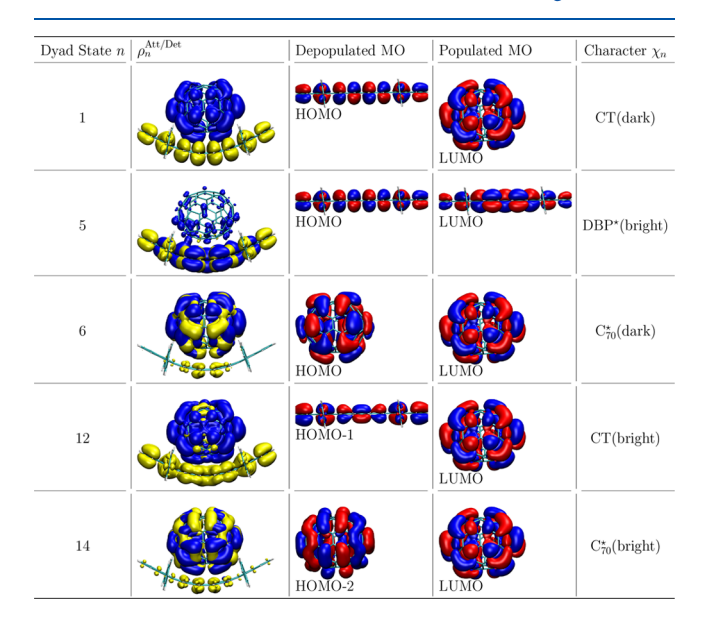


**Figure 4.** Characterization of dyad states based on single molecular orbitals (MOs). For the full table, see Section S1 of the Supporting Information.

provided for the full set in Section S1 of the Supporting Information. The excitation energies of the 25 excited dyad states at the electronic ground-state equilibrium geometry are also shown in Figure 5a, where the different state characters are indicated by different colors.

Importantly, the transition energies generated by our SRSH-PCM methodology are consistent with the corresponding peaks in the experimental absorption spectra. To demonstrate this, we compare in Table 2 DBP excitation energies calculated using different density functionals with the corresponding exper-

imental values, which were adopted from ref 7. It should be noted that the RSH-PCM calculations based on the  $\omega$ PBE functional overestimate the energy gaps. In contrast, the SRSH-PCM methodology appears to reproduce the experimental transition frequencies and relative peak heights (inferred from the calculated oscillator strengths) rather well. We also point out that while the B3LYP-based transition frequencies are in reasonable agreement with experiment, the corresponding oscillator strengths are not. We therefore proceed with the SRSH-PCM-based values. While this work focuses on simulating the electronic dynamics within a DBP-C70 dyad model system, a similar computational framework has been successfully applied recently in ref 7 to interpret experimental time-resolved spectroscopic measurements in thin-film DBP-C70 samples and trace them back to the important role both donor and acceptor excitons play in charge separation.

To assess the validity of the harmonic approximation and the quality of the calculated HRFs, we considered two states for which the optimized structure could be calculated: The lowest state that is a CT dyad state and the locally excited DBP state present the lowest state with significant oscillator strength. In both cases the agreement between directly calculating the reorganization energy to that based on monomer displacements is within 0.02 eV. The DBP locally excited dyad state is found to have a reorganization energy of 0.21 eV, while the DBP single molecule HRFs obtained for the displacement between the neutral to excited state geometries is 0.23 eV. The first CT dyad state has a reorganization energy of 0.18 eV, and is reproduced well using the monomer HRFs with a 0.19 eV. The HRFs are based on the monomer displacements between the neutral to cation geometries for DBP, and between the neutral to anion geometries for C70.

**Transition States Kinetics.** Transition rate constants were calculated between all calculated dyad states. A comprehensive list of all six hundred transition rate constants  $\{k_{mn}^{\xi}\}$  is provided in the Supporting Information, Section S3, where we also list the corresponding electronic coupling coefficients,  $\{V_{mn}\}$ , reaction energies,  $\{\Delta E_{mn}\}$ , and reorganization energies,  $\{E_{mn}^{\xi}\}$ .

The dynamics of electronic energy and charge transfer was obtained by numerically solving the master equation, eq 3, with initial conditions that correspond to starting at different bright excited states. To this end, a time step of 0.001 fs was used. The results of the simulations show that the two target CT states (states n = 1, 2, colored black in Figure 5a) are populated within  $\sim 1$  ps, regardless of the initial state. However, the pathways to those target states were found to be rather sensitive to the choice of the initial state, with the possibility of multiple pathways for the same initial state.

To demonstrate this, we consider the pathways that correspond to starting at four different bright excited states: State 5, which corresponds to a localized excitation on DBP, states 17 and 22 which correspond to a localized excitation on  $C_{70}$ , and state 21, which has a significant CT character (see panels b—e in Figure 5).

Figure 5b shows the kinetics that correspond to starting from state n = 5 (colored red in Figure 5a). The CT process in this case is dominated by two pathways that correspond to direct electron transfer into the final CT states m = 1, 2 (colored black in Figure 5b), without intermediate steps. The corresponding transition rate constants are  $k_{1,5}^{\text{FGR}} = 1.0 \times 10^{12} \text{ s}^{-1}$  (inverted region) and  $k_{2,5}^{\text{FGR}} = 7.0 \times 10^{11} \text{ s}^{-1}$  (normal region). Another significant, although less efficient, pathway is through an intermediate uphill transition to  $C_{70}$ -localized state 6. However,

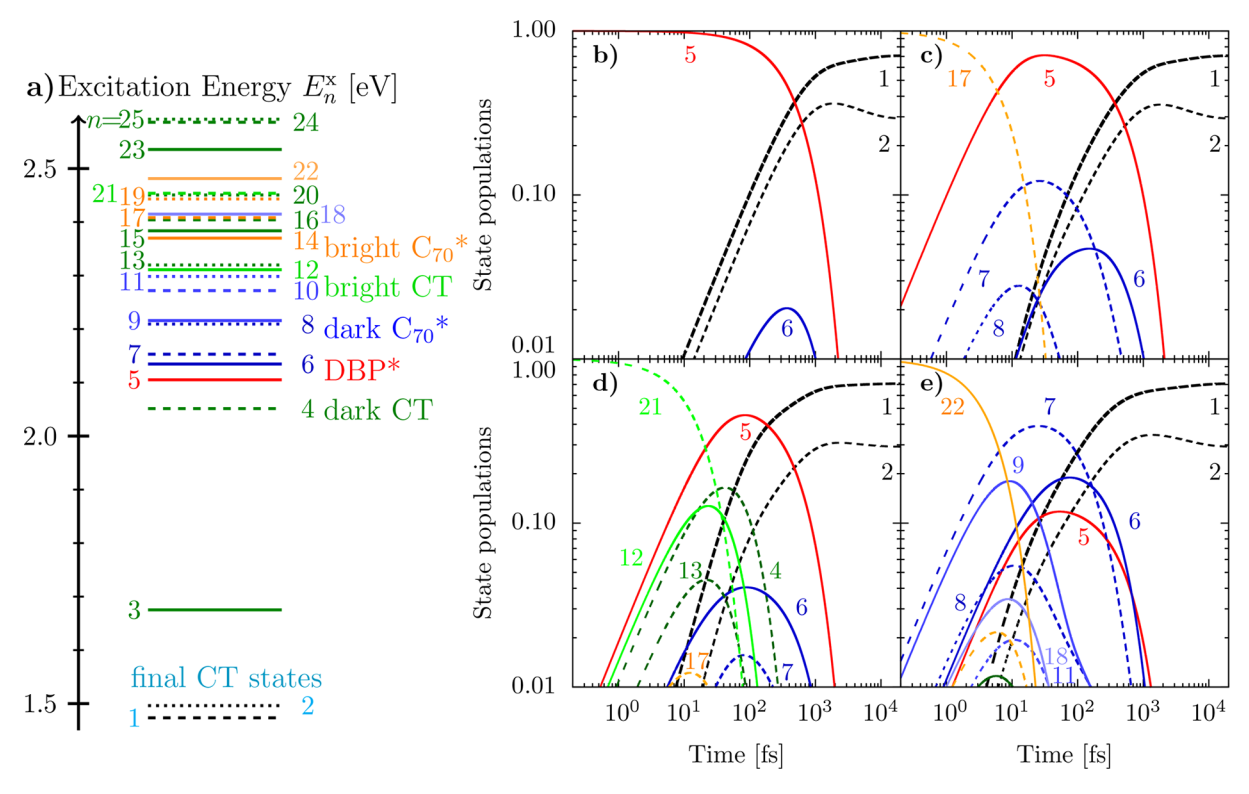


Figure 5. Panel a. Energy level diagram of the interfacial dyad states shown to scale at the ground state equilibrium geometry. Characters of the states are indicated by color. Panels b—e. Kinetics starting from states 5, 17, 21, and 22, respectively.

Table 2. Calculated DBP Monomer Excitation Energies (in eV) of Significant Oscillator Strength in Gas-Phase (g) and Solvated via PCM (s) Compared against the Energies of the Measured Spectral Peaks of a DBP Thin Film (tf) Taken from Ref  $7^a$ 

Method	medium	1. peak	2. peak	3. peak
Exp.	tf	2.0	3.6	4.0
B3LYP	g	2.25 (1.19)	3.86 (1.26)	4.36 (0.4)
B3LYP	S	2.17 (1.41)	3.84 (1.22)	$4.31 \ (0.26^{b})$
RSH	g	2.43 (1.31)	4.29 (1.46)	4.82 (0.83)
RSH	s	2.26 (1.57)	4.19 (1.96)	4.77 (1.16)
SRSH	s	2.11 (1.46)	3.84 (1.66)	4.35 (0.74)

"Values in parentheses represent calculated oscillator strengths. "Two near degenerate lines of comparable oscillator strengths are found.

the corresponding transition rate constant is  $k_{6,5}^{\rm FGR} = 1.1 \times 10^{11}$  s<sup>-1</sup>, which is an order of magnitude smaller than  $k_{1,5}^{\rm FGR}$  and  $k_{2,5}^{\rm FGR}$ .

Figure 5c shows the kinetics that correspond to starting from the  $C_{70}$ -localized state n = 17 (colored orange in Figure 5a). An early rapid increase of the population of the transient DBPlocalized m = 5 state (colored red in Figure 5c) is notable, which can be traced back to a highly efficient DBP-to-C<sub>70</sub> Förster resonant energy transfer ( $k_{5,17}^{FGR} = 1.1 \times 10^{14} \text{ s}^{-1}$ ). Competing pathways involve intramolecular relaxation within  $C_{70}$  into lower dark  $C_{70}$ -localized states m = 6, 7, and 8 (colored blue in Figure 5c), with transition rate constants up to  $k_{7,17}^{\text{FGR}} = 1.8 \times 10^{13} \text{ s}^{-1}$ . A subsequent exciton transfer from these dark C<sub>70</sub>-localized states to DBP was not observed. This can be traced back to significantly weaker electronic coupling coefficients  $V_{5,n}$  of the dark  $C_{70}$  states (n = 6, 7, and 8), which are in the range of 1 to 10 meV. The bright states (n = 14, 17, 19, and 22), on the other hand, show coupling coefficients between 25 and 150 meV, which rank among the highest electronic coupling values found

in this system (see the full table in Supporting Information, Section S3).

Figure 5c also shows efficient transitions via hole transfer between the transiently populated  $C_{70}$  dark states, n=6, 7, 8 (colored blue in Figure 5a) and the target CT states 1 and 2 (colored black Figure 5c), with the corresponding rate constants given by  $k_{2,6}^{FGR} = 1.4 \times 10^{12} \, \mathrm{s}^{-1}$ ,  $k_{1,7}^{FGR} = 4.4 \times 10^{12} \, \mathrm{s}^{-1}$ , and  $k_{2,8}^{FGR} = 1.5 \times 10^{13} \, \mathrm{s}^{-1}$ . It should be noted that these hole transfer rate constants (transition between  $C_{70}$ -localized states 6,7,8 and the target CT states) are *only* slightly faster than the electron transfer rate constants (transitions for state 5 to states 1 and 2) due to the relative values of the electronic coupling coefficients that are quite similar. Yet, hole transfer is more dominant due to the larger density of states of  $C_{70}$  [i.e., the fact that there are three parent states (6, 7, 8) for hole transfer vs one parent state for electron transfer (5)]. Thus, the slightly more efficient hole transfer pathway is the result of the larger density of states of the  $C_{70}$  molecule rather than stronger electronic coupling.

Figure 5e shows the kinetics that correspond to starting from another  $C_{70}$ -localized excited state, n=22 (colored orange in Figure 5a). In contrast to state n=17 (panel c), transitions into multiple dark  $C_{70}$  states (colored blue in Figure 5a), corresponding to intramolecular relaxation, are significantly faster in this case than the transfer of the competing exciton to DBP (colored red in Figure 5a). Starting in either of the two other bright  $C_{70}$ -localized excited states, n=14, 19, and 19, respectively, yields a similar behavior (not shown). The sensitivity of the pathway to the initial state, even when the initial states are of similar character (for example, the n=17 and 22 states), suggests that the pathway may be controlled by selective photoexcitation.

Finally, Figure 5d shows the kinetics that correspond to starting from the n = 21 excited state (colored bright green in Figure 5a). This state has a significant oscillator strength ( $\Omega_{21}$  =

0.022) as well as a significant CT character ( $dQ_{21} = 1.5 e$ ), and it gives rise to several competing pathways. Somewhat surprisingly, the most efficient pathway involves transient charge recombination by a transition to state m = 5, with a rate constant of  $k_{5,21}^{\text{FGR}} = 1.9 \times 10^{13} \text{ s}^{-1}$ . Other, somewhat less efficient pathways maintain the CT character of the initial state, n = 21, and involve transitions to the other bright CT state, m = 12 (colored bright green in Figure 5a) or dark CT states, m = 4, 13 (colored dark green in Figure 5a). The transition rate constants to those three states are relatively fast and rather similar  $(10^{12} - 10^{13} \text{ s}^{-1})$ . The electronic coupling coefficients of all of the aforementioned transitions are similar. The slightly higher value of  $k_{5,21}^{FGR}$  can be traced back to the fact that this transition is in the inverted region, and thereby enhanced by quantum tunneling. Importantly, accounting for this nuance calls for a post-Marcus approach. Indeed, the corresponding Marcus rate constant,  $k_{5,21}^{M}$ , is an order of magnitude *smaller* than the Marcus rate constants of the competing transitions,  $k_{m,21}^{\rm M}$  with m=4,12,13 (see full table of the rate constants in Supporting Information, Section S3). This case therefore represents an example for a situation where the pathways predicted by Marcus theory would be qualitatively wrong.

Another notable, yet less efficient, CT pathway that can be discerned from Figure 5d is via dark  $C_{70}$ -localized state 6 as an intermediate (colored blue in Figure 5d). Its occurrence indicates a temporary charge recombination via hole transfer with a rate constant of  $k_{6,21}^{\rm FGR} = 2.1 \times 10^{12} \, {\rm s}^{-1}$ . The fact that this pathway is less efficient implies that charge recombination via electron back-transfer (discussed in the previous paragraph) is more efficient than via hole backtransfer. This can be traced back to the weaker electronic coupling coefficient in the latter case. Electron backtransfer involves transitions between higher-lying LUMOs, whereas hole backtransfer involves transitions between lower-lying HOMOs, see Figure 3. Thus, the lower electronic coupling is likely due to the more localized nature of the HOMOs compared to the LUMOs, which results in a lower orbital overlap.

**Population Transfer Kinetics.** Next, we consider the dependence of the CT efficiency on whether one starts with photoexcitation by DBP (donor) or  $C_{70}$  (acceptor). To this end, simulations of the kinetics were performed, where the initial state is either the DBP-localized excited state (n = 5) or a combination of the bright  $C_{70}$ -localized excited states (n = 14, 17, 19, 22), where the initial state occupancies are determined based on the relative oscillator strengths. For completeness, starting with the two bright CT excited states is also considered. For the sake of this analysis, the populations of the target CT states are grouped together.

The kinetics of the populations of states grouped based on their character are shown in Figure 6. An effective CT rate constant  $k_\chi^{\rm eff}$ ,  $\chi \in \{{\rm DBP^*}, {\rm C}_{70}^*, {\rm and CT}\}$  was obtained by fitting the time evolution of the target CT states' population to the following functional form (dashed black curve in Figure 6):

$$F(t) = 1 - \exp(-k_{\chi}^{\text{eff}}t) \tag{35}$$

To help with the interpretation, the gray vertical lines in Figure 6 indicate the time it takes for half of the total population to accumulate in the two target CT states.

A close inspection of Figure 6 reveals that even though CT via electron transfer following the photoexcitation of the donor (DBP) is a direct process that does not involve intermediates, it is also the slowest, and thereby least efficient, CT pathway, with

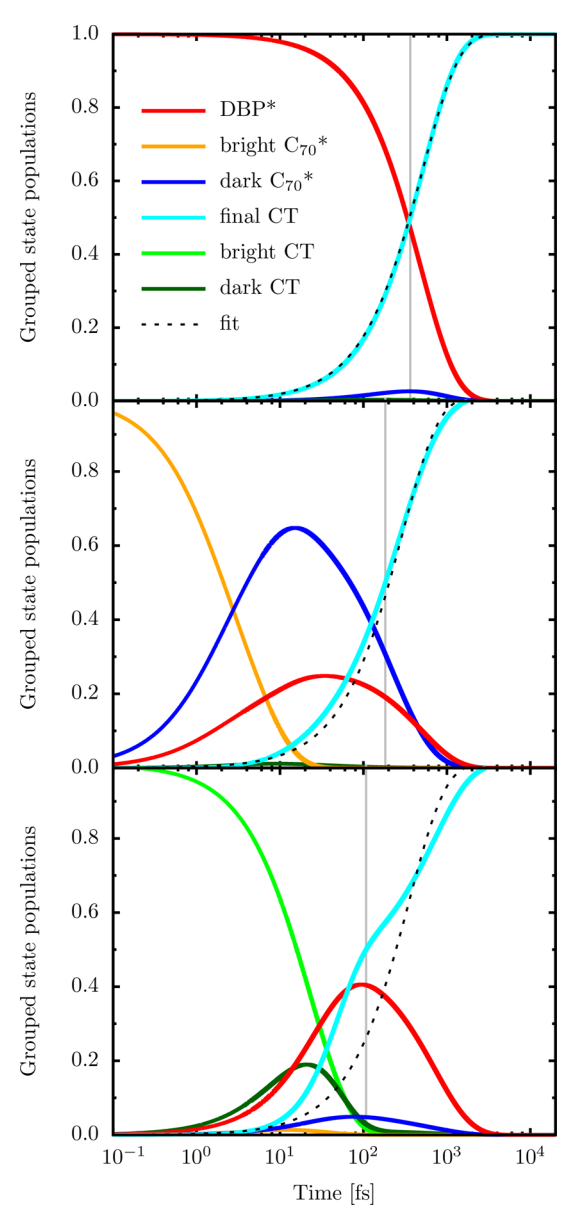


**Figure 6.** Evolving populations of states grouped by their character. An effective CT rate constant  $k_\chi^{\rm eff}$ ,  $\chi \in \{{\rm DBP}^*, C_{00}^*, {\rm and CT}\}$  was obtained by fitting the time evolution of the target CT states' population to the functional form in eq 35 (dashed black curves). The gray vertical lines indicate the time it takes for half of the total population to accumulate in the two target CT states.

an effective rate constant of  $k_{\mathrm{DBP}^*}^{\mathrm{eff}} = 1.9 \times 10^{12} \ \mathrm{s}^{-1}$  (Figure 6, upper panel). In contrast, despite the fact that CT via hole transfer following the photoexcitation of the bright  $C_{70}$  states is an indirect process that involves intermediates, it is faster, and thereby more efficient with an effective rate constant of of  $k_{C_{70}}^{\mathrm{eff}} = 3.4 \times 10^{12} \ \mathrm{s}^{-1}$  (Figure 6, middle panel). Finally, as expected, the fastest, and thereby most efficient, CT pathway starts out with photoexcitation of the bright excited CT states, with an effective CT rate constant of  $k_{\mathrm{CT}}^{\mathrm{eff}} = 2.8 \times 10^{12} \ \mathrm{s}^{-1}$  (Figure 6, lower panel). In this case, CT occurs via multiple pathways, including intermediate CT states (dark green curve), via electron back-transfer into a donor-localized excited state (red curve), and via hole back-transfer into an acceptor-localized excited state (blue curve).

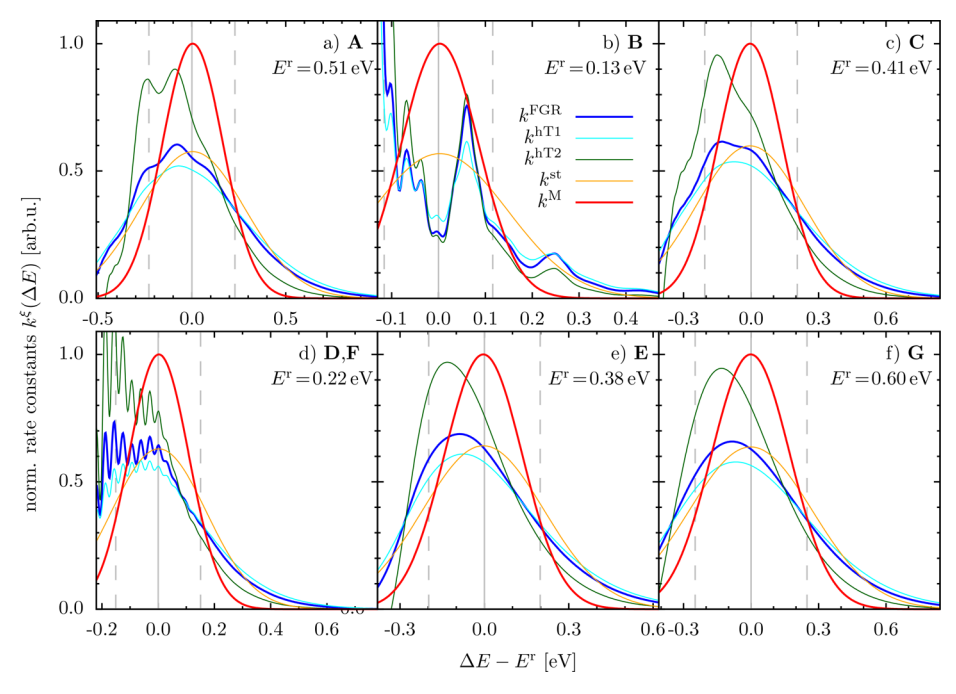


Figure 7. A comparison between the quantum mechanically exact FGR rate constant and four approximate versions of it. Different panels correspond to the different types of electronic transitions labeled A-G (see Figure 3). Each panel shows the FGR rate constant and its approximations (normalized with respect to the maximum of the Marcus theory rate constant) as a function of  $\Delta E - E_r$ . The solid gray vertical line in each panel corresponds to the value of  $\Delta E$  where the activation energy vanishes,  $E^A = 0$ . The two dashed vertical gray lines correspond to the values of  $\Delta E$ , where the activation energy is equal to  $k_B$  T,  $E^A = k_B$  T (in the normal and inverted regions).

**Transition Rate Theory.** The analysis until this point was based on rate constants obtained within the fully quantum-mechanical FGR framework (eq 5). In the next step, we consider the validity of different approximate versions of the FGR rate constants (see eqs 10 and 14) and their effect on the CT rates and pathways.

A comparison between the quantum mechanically exact FGR rate constant and four approximate versions of it is shown in Figure 7. Different panels in this figure correspond to the aforementioned different types of electronic transitions labeled A–G (see Figure 3). Each panel shows the FGR rate constant and its approximate versions (normalized with respect to the maximum of the Marcus theory rate constant) as a function of  $\Delta E - E_r$ , where  $\Delta E$  is varied and  $E_r$  is determined by the considered character and the relevant HRFs. The solid gray vertical line in each panel corresponds to  $\Delta E - E_r = 0$ , where the activation energy is vanishing,  $E^A = 0$  (see eq 15). ( $\Delta E - E_r = 0$  also corresponds to the transition between the normal and inverted regions.) The two dashed vertical gray lines correspond the  $E_r$ , where the activation energy is equal to  $k_B T$ ,  $E^A = k_B T$  (in the normal and inverted regions).

A close inspection of Figure 7 reveals the following trends:

- First, comparison of the hT1 approximation (cyan curves) to the exact rate constant (blue curves) reveals broadening and lowering of the former relative to the latter, with the location of the maximum unaltered. This results in a slight underestimation for small values of  $|\Delta E E^{\rm r}|$  and a slight overestimation for larger values of  $|\Delta E E^{\rm r}|$ .
- Second, comparison of the hT2 approximation (green curves) to the exact rate constant (blue curves) reveals the opposite trend, where the former is narrower and larger relative to the latter, with the location of the maximum unaltered. It is also noteworthy that both hT1 and hT2 approximations are able to reproduce the structure seen in

- the dependence of the exact FGR rate constant on  $\Delta E E^{r}$  (see panels a d of Figure 7). The peaks in this structure can be traced back to the frequencies of modes with large HRFs.
- Third, unlike the exact, hT1, and hT2 rate constants, the rates based on short time (st) approximation present a smooth Gaussian shape that appear structureless (orange curves). While the width and maximum value of the Gaussian function are comparable to those of the exact FGR rate constant, the maximum is at  $\Delta E E^{\rm r} = 0$ , where the activation energy  $E^{\rm A}$  vanishes.
- Fourth, the Marcus theory approximation is seen to retain the Gaussian form, but it is narrower and larger than the st approximation, with the maximum still at  $\Delta E E^{\rm r} = 0$  (red curves). The turning point between overestimated and underestimated rate constants relative to the exact result is around  $E^{\rm A} = k_{\rm B}T$  in the inverted region, and at  $E^{\rm A} < k_{\rm B}T$  in the normal region. (Panel b presents a slight exception due to the more pronounced structure caused by the relatively small number of modes with significant HRFs in DBP.)

Further insight can be obtained by distinguishing between rate constants that fall within the normal region (labeled "n"),  $\Delta E_{mn} \geq E_{mn}^{\rm r}$ , and constants that fall within the inverted region (labeled "i"),  $\Delta E_{mn} < E_{mn}^{\rm r}$ . Among the 300 calculated downhill transition rate constants, 199 were found to fall within the normal region and 101 were found to fall within the inverted region. When it comes to approximations, the hT2 approximation was observed to exhibit nonphysical behavior in some cases. More specifically, 29 out of the 300 hT2 rate constants, all in the normal region with low values of  $\Delta E_{mn}$ , were found to have negative numerical values, which are clearly nonphysical and were therefore not taken into account in the following analysis. Such artifacts do not occur for any of the other approximations.

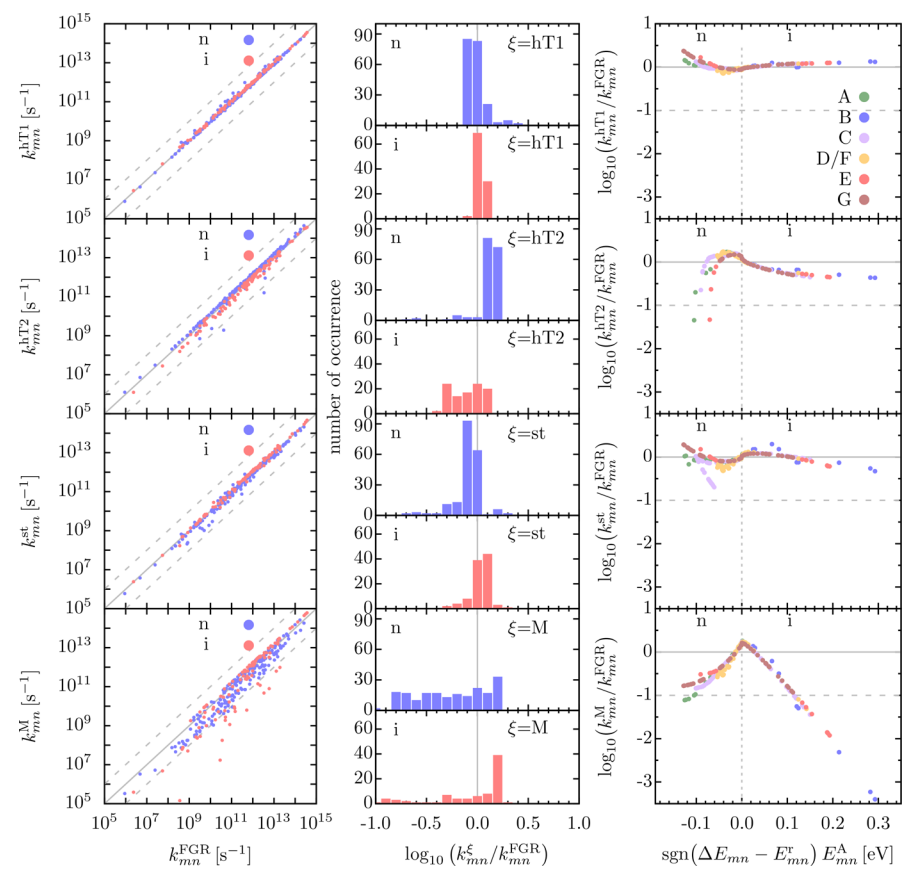


**Figure 8.** Left panels: log—log correlation plots of the 300 exact vs approximate rate constants for the four approximations under consideration. Rate constants for transitions in the normal (inverted) region are shown in blue (red) color. The solid diagonal gray lines indicate 100% agreement between the exact and approximate rate constants. The dashed diagonal lines mark deviations by a factor of 10 in either direction. Middle panels: Histograms of  $\log_{10}(k_{mn}^{E}/k_{mn}^{FGR})$ , with the bin size set to 0.01 (in the normal and inverse regions) and the range corresponding to the area between the dashed gray lines in the left column. Right panels: Correlation plots between  $\log_{10}(k_{mn}^{E}/k_{mn}^{FGR})$  and the activation energy,  $E_{mn}^{A}$ , eq 15.

A comparison of the 300 exact rate constants with the corresponding four approximations,  $\xi \in \{hT1, hT2, st, and M\}$ , is shown in Figure 8. In the figure, rate constants in the normal region are shown in blue and those in the inverted region are shown in red. The left column of Figure 8 shows log-log correlation plots of the 300 exact vs approximate rate constants for the four approximations under consideration. The solid diagonal gray lines indicate 100% agreement between the exact and approximate rate constants. Points above this line correspond to the approximate rate constant being overestimated, while points below this line correspond to the approximate rate constant being underestimated. The dashed diagonal lines mark deviations by a factor of 10 in either direction. The middle column of Figure 8 shows histograms of  $\log_{10}(k_{mn}^{\xi}/k_{mn}^{\text{FGR}})$ , with the bin size set to 0.01 (in the normal and inverse regions) and the range corresponding to the area between the dashed gray lines in the left column.

Inspection of Figure 8 reveals the following trends:

- The deviations of the hT1 approximation from the exact rate constant are rather small (first row in Figure 8). When it comes to trends, transition rate constants in the inverted regime tend to be slightly overestimated by hT1, while those in the normal regime tend to be slightly underestimated.
- The deviations of the hT2 approximation from the exact rate constant are larger in comparison to the hT1 approximation (second row in Figure 8). The deviations

- in the case of hT2 also follow an opposite trend compared to hT1; namely, transition rate constants in the inverted regime tend to be underestimated by hT2, while those in the normal regime tend to be overestimated.
- The deviations of the st approximation from the exact rate constant are seen to be relatively small (third row in Figure 8). Transition rate constants in the inverted regime tend to be overestimated by st, while those in the normal regime tend to be underestimated.
- The deviations of the Marcus approximation from the exact rate constant are seen to be significantly larger (fourth row in Figure 8). Transition rate constants in the inverted regime tend to be overestimated by the Marcus approximation, while those in the normal regime tend to be underestimated. Interestingly, although Marcus theory corresponds to the combination of the hT2 and st approximations, the above-mentioned opposite trends seen for the hT2 and st approximations do not compensate for each other in this case.

The trends observed in the high temperature limits can be rationalized by closely inspecting the corresponding rate expressions in eqs 5, (10), and (11). In the exact expression, the phonon density  $n_{\alpha}$  — which is accompanied by an added constant—appears within a product with the corresponding HRF  $S_{\alpha}$ . In the hT1 limit, this product is slightly increased by the phonon density substitution, whereas it is significantly decreased (in particular, for larger frequencies) by neglecting the

additional constant within the hT2. A very similar, yet not fully equivalent, outcome for the product would be obtained if the HRFs in the exact expression would be increased (hT1) or decreased (hT2), respectively. Thus, the hT1 limit resembles an energy landscape in which the activation energy is increased in the normal region and decreased in the inverted region, and vice versa in the hT2 limit.

The trends found in the st approximation are traced back to the simplified temporal behavior of the integrand in the approximated rate expression, eq 12, and the thus effectively reduced integration time window, which suppresses resonance and tunneling effects.

Another perspective can be obtained by examining the correlation plots between  $\log_{10}(k_{\rm m}^{\rm E}/k_{\rm mn}^{\rm FGR})$  and the activation energy,  $E_{\rm mn}^{\rm A}$ , eq 15 (see right column in Figure 8). Here, different colors are assigned to the seven different types of transitions defined in Figure 3. Rate constants for the same transition type share the same set of HRFs,  $\{S_{\alpha}^{X_{\rm mn}}\}$  and therefore give rise to the same  $\kappa_{\rm mn}^{\rm E}(t)$  (see eq 5). Inspection of the four panels on the right column of Figure 8 reveals that the  $\log_{10}(k_{\rm mn}^{\rm E}/k_{\rm mn}^{\rm FGR})$  is correlated with  $E^{\rm A}$ . The correlation between  $\log_{10}(k_{\rm mn}^{\rm E}/k_{\rm mn}^{\rm FGR})$  and  $E^{\rm A}$  is rather insensitive to the transition type in the inverted region. However, the sensitivity of the correlation to the type of transition can be observed in the normal region.

The correlation between log  $_{10}(k_{mn}^M/k_{min}^{\rm FGR})$  and  $E_{mn}^{\rm A}$  in the Marcus case is noteworthy. The deviations from the exact rate constant are significantly larger in the inverted region, with log  $_{10}(k_{mn}^M/k_{mn}^{\rm FGR})$  linearly and negatively correlated with  $E_{mn}^{\rm A}$ , which is attributed to the enhanced role of tunneling with increasing activation energy in the inverted region. Smaller deviations are seen in the normal region, which are also observed to be linearly and negatively correlated with minor deviations from linearity at larger activation energies.

Another noteworthy trend that can be inferred from the Marcus case on the right column of Figure 8 is that while most points satisfy  $k_{mn}^M < k_{mn}^{\rm FGR}$ , there is a significant number of points for which  $k_{mn}^M > k_{mn}^{\rm FGR}$ . The latter instance is seen to be correlated with small activation energies, and can be traced back to the hT2 approximation in the normal region <sup>78</sup> and the st approximation in the inverted region.

## SUMMARY

To summarize, in this paper, we presented a comprehensive computational analysis of the electronic transition rates and pathways that underlie charge separation in the DBP: $C_{70}$  interfacial dyad following photoexcitation. Our analysis was based on a computational framework that combines FGR rate theory with polarization-consistent DFT inputs obtained via our SRSH-PCM method, which is meant to account for the effect of the solid state environment and generate reliable electronic energy levels.

Multiple charge separation pathways that involve various combinations of electron and hole transfer and backtransfer, exciton transfer, and internal relaxation steps have been identified. Most notably, we have found that multistep transition pathways via intermediate states (including dark states) often outcompete direct transfer pathways and that intermolecular charge and energy transfer can be significantly faster than the intramolecular internal conversion relaxation process. Our analysis is consistent with the experimental observation  $^{7,8}$  that photoexciting the acceptor ( $C_{70}$ ) can be somewhat more effective at triggering charge separation (via a hole transfer) than photoexciting the donor (DBP, via electron transfer). Our

analysis also points to the larger density of states of  $C_{70}$ , compared to that of DBP, as the origin for the slightly larger efficiency of the hole transfer mechanism.

We also presented a detailed analysis of the validity of various high-temperature and short-time approximations of the FGR rate constant with Marcus theory (i.e., the combination of the high-temperature and short-time approximations) corresponding to the most approximate version. While those approximate versions were found to reproduce most transition rate constants rather well, notable deviations have been observed for a significant number of them, particularly in the case of Marcus theory. More specifically, a significant number of Marcus theory rate constants were seen to either underestimate (due to their inability to account for tunneling) or overestimate (in the case of transitions with a low activation energy) the fully quantum-mechanical FGR transition rate constants. This observation suggests that caution is called for when assuming that the Marcus rate theory is generally valid for all electronic transitions.

### ASSOCIATED CONTENT

# Supporting Information

The Supporting Information is available free of charge at https://pubs.acs.org/doi/10.1021/acs.jpclett.3c01927.

HRFs of all the single molecule displacements, characterization of the dyad states, and the full rate constants table (PDF)

Transparent Peer Review report available (PDF)

# AUTHOR INFORMATION

# **Corresponding Authors**

Eitan Geva — Department of Chemistry, University of Michigan, Ann Arbor, Michigan 48109, United States; orcid.org/ 0000-0002-7935-4586; Email: eitan@umich.edu Barry D. Dunietz — Department of Chemistry and Biochemistry, Kent State University, Kent, Ohio 44242, United States;

orcid.org/0000-0002-6982-8995; Email: bdunietz@kent.edu

### **Authors**

Alexander Schubert — Department of Chemistry, University of Michigan, Ann Arbor, Michigan 48109, United States; Department of Chemistry and Biochemistry, Kent State University, Kent, Ohio 44242, United States; Present Address: Merck Electronics KGaA, 64293 Darmstadt, Germany; orcid.org/0000-0002-8560-6436

Srijana Bhandari — Department of Chemistry and Biochemistry, Kent State University, Kent, Ohio 44242, United States

Complete contact information is available at: https://pubs.acs.org/10.1021/acs.jpclett.3c01927

### Notes

The authors declare no competing financial interest.

# ACKNOWLEDGMENTS

We thank Prof. Jennifer Ogilvie (University of Michigan) for useful discussions. B.D.D. and E.G. are grateful for joint support by U.S. Department of Energy, Office of Basic Energy Sciences, under Award Number DE-SC0016501. E.G. acknowledges support by NSF via Grant CHE-2154114. We are also thankful to the Ohio Supercomputer Center<sup>79</sup> and the Kent State University College of Arts and Sciences for computing facilities

and making the resources available to complete the reported research.

# REFERENCES

- (1) Clarke, T. M.; Durrant, J. R. Charge Photogeneration in Organic Solar Cells. *Chem. Rev.* **2010**, *110*, *6736*.
- (2) Few, S.; Frost, J. M.; Nelson, J. Models of Charge Pair Generation in Organic Solar Cells. *Phys. Chem. Chem. Phys.* **2015**, *17*, 2311.
- (3) Bakulin, A. A.; Dimitrov, S. D.; Rao, A.; Chow, P. C. Y.; Nielsen, C. B.; Schroeder, B. C.; McCulloch, I.; Bakker, H. J.; Durrant, J. R.; Friend, R. H. Charge-Transfer State Dynamics Following Hole and Electron Transfer in Organic Photovoltaic Devices. *J. Phys. Chem. Lett.* **2013**, *4*, 209
- (4) Xiao, X.; Zimmerman, J. D.; Lassiter, B. E.; Bergemann, K. J.; Forrest, S. R. A Hybrid Planar-Mixed Tetraphenyldibenzoperiflanthene/C70 Photovoltaic Cell. *Appl. Phys. Lett.* **2013**, *102*, No. 073302.
- (5) Hendriks, K. H.; Wijpkema, A. S. G.; van Franeker, J. J.; Wienk, M. M.; Janssen, R. A. J. Dichotomous Role of Exciting the Donor or the Acceptor on Charge Generation in Organic Solar Cells. *J. Am. Chem. Soc.* 2016, 138, 10026.
- (6) Ding, K.; Liu, X.; Forrest, S. R. Charge Transfer and Collection in Dilute Organic Donor—Acceptor Heterojunction Blends. *Nano Lett.* **2018**, *18*, 3180.
- (7) Song, Y.; Schubert, A.; Liu, X.; Bhandari, S.; Forrest, S. R.; Dunietz, B. D.; Geva, E.; Ogilvie, J. P. Efficient Charge Generation via Hole Transfer in Dilute Organic Donor—Fullerene Blends. *J. Phys. Chem. Lett.* **2020**, *11*, 2203–2210.
- (8) Liu, X.; Ding, K.; Panda, A.; Forrest, S. R. Charge Transfer States in Dilute Donor—Acceptor Blend Organic Heterojunctions. *ACS Nano* **2016**, *10*, 7619.
- (9) Dexter, D. L. A Theory of Sensitized Luminescence in Solids. J. Chem. Phys. 1953, 21, 836–850.
- (10) Dexter, D. L.; Schulman, J. H. Theory of Concentration Quenching in Inorganic Phosphors. *J. Chem. Phys.* **1954**, 22, 1063–1070.
- (11) Förster, T. Zwishenmolekulare Energiewanderung und Fluoreszenz. *Ann. Physik* **1948**, *437*, 55.
- (12) Lee, M. H.; Dunietz, B. D.; Geva, E. Calculation from First Principles Intramolecular Golden-rule rate constants for Photoinduced Electron Transfer in Molecular Donor-Acceptor Systems. *J. Phys. Chem.* C 2013, 117, 23391–23401.
- (13) Lee, M. H.; Dunietz, B. D.; Geva, E. Donor-to-Donor vs Donor-to-Acceptor Interfacial Charge Transfer States in the Phthalocyanine—Fullerene Organic Photovoltaic System. *J. Phys. Chem. Lett.* **2014**, *5*, 3810—3816.
- (14) Lee, M. H.; Geva, E.; Dunietz, B. D. Calculation from First-Principles of Golden Rule Rate Constants for Photoinduced Subphthalocyanine/Fullerene Interfacial Charge Transfer and Recombination in Organic Photovoltaic Cells. *J. Phys. Chem. C* **2014**, *118*, 9780–9789.
- (15) Bhandari, S.; Cheung, M.; Geva, E.; Kronik, L.; Dunietz, B. D. Fundamental Gaps of Condensed-Phase Organic Semiconductors From Single-Molecule Polarization-Consistent Optimally Tuned Screened Range-Separated Hybrid Functionals. *J. Chem. Theory Comput.* 2018, 14, 6287–6294.
- (16) Bhandari, S.; Dunietz, B. D. Quantitative Accuracy in Calculating Charge Transfer State Energies in Solvated Molecular Dimers Using Screened Range Separated Hybrid Functional Within a Polarized Continuum Model. *J. Chem. Theory Comput.* **2019**, *15*, 4305.
- (17) Aksu, H.; Schubert, A.; Geva, E.; Dunietz, B. D. Explaining Spectral Asymmetries and Excitonic Characters of the Core Pigment Pairs in the Bacterial Reaction Center Using Screened Range-Separated Hybrid Functionals. *J. Phys. Chem. B* **2019**, *123*, 8970–8975.
- (18) Aksu, H.; Schubert, A.; Bhandari, S.; Yamada, A.; Geva, E.; Dunietz, B. D. On the Role of the Special Pair in Photosystems as a Charge Transfer Rectifier. *J. Phys. Chem. B* **2020**, *124*, 1987–1994.
- (19) Chakravarty, C.; Aksu, H.; Maiti, B.; Dunietz, B. D. Electronic Spectra of C60 Films Using Screened Range Separated Hybrid Functionals. *J. Phys. Chem. A* **2021**, *125*, 7625–7632.

- (20) Perdew, J. P.; Levy, M. Physical Content of the Exact Kohn-Sham Orbital Energies: Band Gaps and Derivative Discontinuities. *Phys. Rev. Lett.* **1983**, *51*, 1884–1887.
- (21) Sham, L. J.; Schlüter, M. Density Functional Theory of the Gap. *Phys. Rev. Lett.* **1983**, *51*, 1888–1891.
- (22) Seidl, A.; Görling, A.; Vogl, P.; Majewski, J. A.; Levy, M. Generalized Kohn-Sham Schemes and the Band-Gap Problem. *Phys. Rev. B* **1996**, *53*, 3764–3774.
- (23) Tozer, D. J. Relationship Between Long-Range Charge-Transfer Excitation Energy Error and Integer Discontinuity in Kohn-Sham Theory. *J. Chem. Phys.* **2003**, *119*, 12697–12699.
- (24) Teale, A. M.; De Proft, F.; Tozer, D. J. Orbital Energies and Negative Electron Affinities From Density Functional Theory: Insight From the Integer Discontinuity. *J. Chem. Phys.* **2008**, *129*, No. 044110.
- (25) Kronik, L.; Stein, T.; Refaely-Abramson, S.; Baer, R. Excitation Gaps of Finite-Sized Systems from Optimally Tuned Range-Separated Hybrid Functionals. *J. Chem. Theory Comput.* **2012**, *8*, 1515–1531.
- (26) Chai, J.-D.; Chen, P.-T. Restoration of the Derivative Discontinuity in Kohn-Sham Density Functional Theory: An Efficient Scheme for Energy Gap Correction. *Phys. Rev. Lett.* **2013**, *110*, No. 033002.
- (27) Cohen, A. J.; Mori-Sánchez, P.; Yang, W. Fractional Charge Perspective on the Band Gap in Density-Functional Theory. *Phys. Rev. B* **2008**, *77*, 115123.
- (28) Mori-Sánchez, P.; Cohen, A. J.; Yang, W. Localization and Delocalization Errors in Density Functional Theory and Implications for Band-Gap Prediction. *Phys. Rev. Lett.* **2008**, *100*, 146401.
- (29) Eisenberg, H. R.; Baer, R. A New Generalized Kohn-Sham Method for Fundamental Band-Gaps in Solids. *Phys. Chem. Chem. Phys.* **2009**. *11*. 4674.
- (30) Mori-Sánchez, P.; Cohen, A. J.; Yang, W. Discontinuous Nature of the Exchange-Correlation Functional in Strongly Correlated Systems. *Phys. Rev. Lett.* **2009**, *102*, No. 066403.
- (31) Yang, W.; Cohen, A. J.; Mori-Sánchez, P. Derivative Discontinuity, Bandgap and Lowest Unoccupied Molecular Orbital in Density Functional Theory. *J. Chem. Phys.* **2012**, *136*, 204111.
- (32) Kronik, L.; Neaton, J. B. Excited-State Properties of Molecular Solids from First Principles. *Annu. Rev. Phys. Chem.* **2016**, *67*, 587–616.
- (33) Perdew, J. P.; Yang, W.; Burke, K.; Yang, Z.; Gross, E. K.; Scheffler, M.; Scuseria, G. E.; Henderson, T. M.; Zhang, I. Y.; Ruzsinszky, A.; Peng, H.; Sun, J.; Trushin, E.; Görling, A. Understanding Band Gaps of Solids in Generalized Kohn-Sham Theory. *Proc. Natl. Acad. Sci. U.S.A.* 2017, 114, 2801–2806.
- (34) Tawada, Y.; Tsuneda, T.; Yanagisawa, S.; Yanai, T.; Hirao, K. A Long-Range-Corrected Time-Dependent Density Functional Theory. *J. Chem. Phys.* **2004**, *120*, 8425–8433.
- (35) Baer, R.; Neuhauser, D. Density Functional Theory with Correct Long-Range Asymptotic Behavior. *Phys. Rev. Lett.* **2005**, *94*, No. 043002.
- (36) Yanai, T.; Tew, D. P.; Handy, N. C. A New Hybrid Exchange-Correlation Functional Using Coulomb-Attenuating Method (CAM-B3LYP). *Chem. Phys. Lett.* **2004**, 393, 51–57.
- (37) Kümmel, S.; Kronik, L. Orbital-Dependent Density Functionals: Theory and Applications. *Rev. Mod. Phys.* **2008**, *80*, 3–60.
- (38) Sun, H.; Ryno, S.; Zhong, C.; Ravva, M. K.; Sun, Z.; Körzdörfer, T.; Bredas, J.-L. Ionization Energies, Electron Affinities, and Polarization Energies of Organic Molecular Crystals: Quantitative Estimations from a Polarizable Continuum Model (PCM)-Tuned Range-Separated Density Functional Approach. *J. Chem. Theory Comput.* **2016**, *12*, 2906–2916.
- (39) Sun, H.; Hu, Z.; Zhong, C.; Zhang, S.; Sun, Z. Quantitative Estimation of Exciton Binding Energy of Polythiophene-Derived Polymers Using Polarizable Continuum Model Tuned Range-Separated Density Functional. *J. Phys. Chem. C* **2016**, *120*, 8048–8055.
- (40) Guo, Z.-H.; Hu, Z.-H.; Sun, Z.-R.; Sun, H. Density Functional Theory Studies on Ionization Energies, Electron Affinities, and Polarization Energies of Organic Semiconductors. *Acta Phys.-Chim. Sin* **2017**, *33*, 1171.

- (41) Bhandari, S.; Zheng, Z.; Maiti, B.; Chuang, C.-H.; Porel, M.; You, Z.-Q.; Ramamurthy, V.; Burda, C.; Herbert, J. M.; Dunietz, B. D. What Is the Optoelectronic Effect of the Capsule on the Guest Molecule in Aqueous Host/Guest Complexes? A Combined Computational and Spectroscopic Perspective. J. Phys. Chem. C 2017, 121, 15481–15488.
- (42) Refaely-Abramson, S.; Sharifzadeh, S.; Jain, M.; Baer, R.; Neaton, J. B.; Kronik, L. Gap Renormalization of Molecular Crystals From Density-Functional Theory. *Phys. Rev. B* **2013**, *88*, No. 081204.
- (43) Zheng, Z.; Egger, D. A.; Brédas, J.-L.; Kronik, L.; Coropceanu, V. Effect of Solid-State Polarization on Charge-Transfer Excitations and Transport Levels at Organic Interfaces From a Screened Range-Separated Hybrid Functional. *J. Phys. Chem. Lett.* **2017**, *8*, 3277–3283.
- (44) Joo, B.; Han, H.; Kim, E.-G. Solvation-Mediated Tuning of the Range-Separated Hybrid Functional: Self-Sufficiency through Screened Exchange. *J. Chem. Theory Comput.* **2018**, *14*, 2823–2828.
- (45) Begam, K.; Bhandari, S.; Maiti, B.; Dunietz, B. D. Screened Range-Separated Hybrid Functional with Polarizable Continuum Model Overcomes Challenges in Describing Triplet Excitations in the Condensed Phase Using TDDFT. J. Chem. Theory Comput. 2020, 16, 3287.
- (46) Song, Y.; Schubert, A.; Maret, E.; Burdick, R. K.; Dunietz, B. D.; Geva, E.; Ogilvie, J. P. Vibronic Structure of Photosynthetic Pigments Probed by Polarized Two-dimensional Electronic Spectroscopy and ab initio Calculations. *Chem. Sci.* **2019**, *10*, 8143–8153.
- (47) MacKenzie, I. A.; Wang, L.; Onuska, N. P. R.; Williams, O. F.; Begam, K.; Moran, A. M.; Dunietz, B. D.; Nicewicz, D. A. Discovery and Characterization of an Acridine Radical Photoreductant. *Nature* **2020**, 580, 76–80.
- (48) Aksu, H.; Maiti, B.; Ptaszek, M.; Dunietz, B. D. Photoinduced Charge Transfer in Zn and Au-Ligated Symmetric and Asymmetric Bacteriochlorin Dyads: A Computational Study. *J. Chem. Phys.* **2020**, *153*, 134111.
- (49) Chakravarty, C.; Aksu, H.; Martinez B., J. A.; Ramos, P.; Pavanello, M.; Dunietz, B. D. Role of Dielectric Screening in Calculating Excited States of Solvated Azobenzene: A Benchmark Study Comparing Quantum Embedding and Polarizable Continuum Model for Representing the Solvent. *J. Phys. Chem. Lett.* **2022**, *13*, 4849.
- (50) Perdew, J. P.; Burke, K.; Ernzerhof, M. Generalized Gradient Approximation Made Simple. *Phys. Rev. Lett.* **1996**, *77*, 3865.
- (51) Chai, J.-D.; Head-Gordon, M. Systematic Optimization of Long-Range Corrected Hybrid Density Functionals. *J. Chem. Phys.* **2008**, *128*, No. 084106.
- (52) Chai, J.-D.; Head-Gordon, M. Long-Range Corrected Hybrid Density Functionals With Damped Atom-Atom Dispersion Corrections. *Phys. Chem. Chem. Phys.* **2008**, *10*, 6615.
- (53) Voityuk, A. A.; Rösch, N. Fragment Charge Difference Method for Estimating Donor—Acceptor Electronic Coupling: Application to DNA  $\pi$ -Stacks. *J. Chem. Phys.* **2002**, *117*, 5607.
- (54) Yang, C.-H.; Hsu, C.-P. A Multi-State Fragment Charge Difference Approach for Diabatic States in Electron Transfer: Extension and Automation. *J. Chem. Phys.* **2013**, *139*, 154104.
- (55) Epifanovsky, E.; et al. Software for the Frontiers of Quantum Chemistry: An Overview of Developments in the Q-Chem 5 Package. *J. Chem. Phys.* **2021**, *155*, No. 084801.
- (56) Niu, Y.; Peng, Q.; Deng, C.; Gao, X.; Shuai, Z. Theory of Excited State Decays and Optical Spectra: Application to Polyatomic Molecules. *J. Phys. Chem. A* **2010**, *114*, 7817–7831.
- (57) Valiev, R. R.; Cherepanov, V. N.; Nasibullin, R. T.; Sundholm, D.; Kurten, T. Calculating Rate Constants for Intersystem Crossing and Internal Conversion in the Franck-Condon and Herzberg-Teller Approximations. *Phys. Chem. Chem. Phys.* **2019**, *21*, 18495–18500.
- (58) Sun, X.; Geva, E. Non-Condon Equilibrium Fermi's Golden Rule Electronic Transition Rate Constants Via The Linearized Semiclassical Method. *J. Chem. Phys.* **2016**, *144*, 244105.
- (59) Sun, X.; Geva, E. Non-Condon Nonequilibrium Fermi's Golden Rule Rates from the Linearized Semiclassical Method. *J. Chem. Phys.* **2016**, *145*, No. 064109.

- (60) Duschinski, F. The importance of the electron spectrum in multi atomic molecules. Concerning Franck—Condon principle. *Acta Physicochim. URSS* **1937**, *7*, 551.
- (61) Etinski, M.; Tatchen, J.; Marian, C. M. Time-Dependent Approaches for the Calculation of Intersystem Crossing Rates. *J. Chem. Phys.* **2011**, *134*, 154105.
- (62) Kananenka, A. A.; Sun, X.; Schubert, A.; Dunietz, B. D.; Geva, E. A Comparative Study of Different Methods for Calculating Electronic Transition Rates. *J. Chem. Phys.* **2018**, *148*, 102304.
- (63) Csehi, A.; Badanko, P.; Halasz, G. J.; Vibok, A.; Lasorne, B. On the Preservation of Coherence in the Electronic Wavepacket of a Neutral and Rigid Polyatomic Molecule. *J. Phys. B: At. Mol. Opt. Phys.* **2020**, 53, 184005.
- (64) Mulvihill, E.; Schubert, A.; Sun, X.; Dunietz, B. D.; Geva, E. A Modified Generalized Quantum Master Equation for Simulating Electronically Nonadiabatic Dynamics. *J. Chem. Phys.* **2019**, *150*, 034101.
- (65) Mulvihill, E.; Gao, X.; Liu, Y.; Schubert, A.; Dunietz, B. D.; Geva, E. Combining the Mapping Hamiltonian Linearized Semiclassical Approach with the Generalized Quantum Master Equation to Simulate Electronically Nonadiabatic Molecular Dynamics. *J. Chem. Phys.* **2019**, *151*, 074103.
- (66) Mulvihill, E.; Lenn, K. M.; Gao, X.; Schubert, A.; Dunietz, B. D.; Geva, E. Simulating Energy Transfer Dynamics in the Fenna-Matthews-Olson Complex via the Modified Generalized Quantum Master Equation. *J. Chem. Phys.* **2021**, *154*, 204109.
- (67) Lee, M. H.; Geva, E.; Dunietz, B. D. The Effect of Interfacial Geometry on Charge-Transfer States in the Phthalocyanine/Fullerene Organic Photovoltaic System. *J. Phys. Chem. A* **2016**, *120*, 2970–2975.
- (68) Manna, A. K.; Dunietz, B. D. Communication: Charge-Transfer Rate Constants in Zinc-Porphyrin-Porphyrin-Derived Dyads: A Fermi Golden Rule First-Principles-Based Study. *J. Chem. Phys.* **2014**, *141*, 121102.
- (69) Wilcox, D. E.; Lee, M. H.; Sykes, M. E.; Niedringhaus, A.; Geva, E.; Dunietz, B. D.; Shtein, M.; Ogilvie, J. P. Ultrafast Charge-Transfer Dynamics at the Boron Subphthalocyanine Chloride/C<sub>60</sub> Heterojunction: Comparison between Experiment and Theory. *J. Phys. Chem. Lett.* **2015**, *6*, 569–575.
- (70) Manna, A. K.; Balamurugan, D.; Cheung, M. S.; Dunietz, B. D. Unraveling the Mechanism of Photoinduced Charge Transfer in Carotenoid Porphyrin C<sub>60</sub> Molecular Triad. *J. Phys. Chem. Lett.* **2015**, *6*, 1231–1237.
- (71) Maiti, B.; Schubert, A.; Sarkar, S.; Bhandari, S.; Wang, K.; Li, Z.; Geva, E.; Twieg, R. J.; Dunietz, B. D. Enhancing Charge Mobilities in Organic Semiconductors by Selective Fluorination: a Design Approach Based on a Quantum Mechanical Perspective. *Chem. Sci.* **2017**, *8*, 6947–6953.
- (72) Sun, X.; Zhang, P.; Lai, Y.; Williams, K. L.; Cheung, M. S.; Dunietz, B. D.; Geva, E. Computational Study of Charge-Transfer Dynamics in the Carotenoid—Porphyrin—C60 Molecular Triad Solvated in Explicit Tetrahydrofuran and Its Spectroscopic Signature. *J. Phys. Chem. C* **2018**, *122*, 11288—11299.
- (73) Maiti, B.; Wang, K.; Bhandari, S.; Bunge, S. D.; Twieg, R. J.; Dunietz, B. D. Enhancing Charge Mobilities in Selectively Fluorinated Oligophenyl Organic Semiconductors: a Design Approach Based on Experimental and Computational Perspectives. *J. Mater. Chem. C* **2019**, 7, 3881.
- (74) Siders, P.; Marcus, R. A. Quantum Effects for Electron-Transfer Reactions in the "Inverted Region. *J. Am. Chem. Soc.* **1981**, *103*, 748–752.
- (75) Marcus, R. A. Electron Transfer Reactions in Chemistry. Theory and Experiment. *Rev. Mod. Phys.* **1993**, *65*, 599–610.
- (76) Jang, S.; Newton, M. D. Closed-Form Expressions of Quantum Electron Transfer Rate Based on the Stationary-Phase Approximation. *J. Phys. Chem. B* **2006**, *110*, 18996–19003.
- (77) Jang, S.; Montoya-Castillo, A. Charge Hopping Dynamics along a Disordered Chain in Quantum Environments: Comparative Study of Different Rate Kernels. *J. Phys. Chem. B* **2015**, *119*, 7659–7665.

- (78) Peskin, U. Quantum Mechanical Averaging Over Fluctuating
- Rates. Mol. Phys. 2012, 110, 729–734.

  (79) Ohio Supercomputer Center. 1987; http://osc.edu/ark:/ 19495/f5s1ph73 Accessed on 01.01.2014.